PHYSICAL REVIEW B **98**, 075138 (2018)

Spin-orbital-lattice entangled states in cubic d^1 double perovskites

Naoya Iwahara,* Veacheslav Vieru, and Liviu F. Chibotaru†

Theory of Nanomaterials Group, University of Leuven, Celestijnenlaan 200F, B-3001 Leuven, Belgium

(Received 19 March 2018; published 21 August 2018)

The interplay of spin-orbit coupling and vibronic coupling on the heavy d^1 site of cubic double perovskites is investigated by *ab initio* calculations. The stabilization energy of spin-orbital-lattice entangled states is found to be comparable to or larger than the exchange interactions, suggesting the presence of Jahn-Teller dynamics in the systems. In Ba_2YMoO_6, the pseudo-Jahn-Teller coupling enhances the mixing of the ground and excited spin-orbit multiplet states, which results in strong temperature dependence of effective magnetic moments. The entanglement of the spin and lattice degrees of freedom induces a strong magnetoelastic response. This multiferroic effect is at the origin of the recently reported breaking of local point symmetry accompanying the development of magnetic ordering in Ba_2NaOsO_6.

DOI: 10.1103/PhysRevB.98.075138

I. INTRODUCTION

Geometrically frustrated systems with strong spin-orbit coupling on metal sites are of great interest in the context of unconventional electronic phases [1,2]. Double perovskites containing heavy d^1 metal ions are candidates for spin liquid systems, the reason for which they have been intensively investigated [3–19]. Although the interplay of spin and orbital degrees of freedom has been widely studied theoretically [20–26], the understanding of the role of lattice degrees of freedom in these systems is lacking. In the cubic d^1 double perovskite Ba_2YMoO_6, in spite of fourfold degeneracy of the local ground multiplet (Γ_8 or effective $J = \frac{3}{2}$), the Jahn-Teller (JT) distortion [27] has not been observed in neutron diffraction measurements down to 2.7 K, which was called a "violation of the JT theorem" [8]. Similarly, x-ray diffraction shows that cubic symmetry of Ba_2AOsO_6 ($A =$ Li, Na) [3] is retained even at 5 K [5], while recent NMR spectra of Ba_2NaOsO_6 suggest the development of "broken local point symmetry" around and below the Curie temperature (≈10 K) [18,19]. The absence of clear-cut JT distortion is most likely explained by either quenching of the JT effect or the presence of the dynamical JT effect. The signs for the latter are seen, for example, in alkali-doped fullerides [28–30] and various metal compounds [31–34]. Since the JT effect can have nontrivial influence on electronic properties, knowledge of its relevance at local metal sites is indispensable for understanding the nature of these materials.

In this work, with the example of three cubic d^1 double perovskites (Ba_2AOsO_6, $A =$ Li, Na, and Ba_2YMoO_6), the local electronic properties generated by the interplay of spin-orbit interaction and vibronic coupling is studied. With the use of coupling parameters derived *ab initio*, the spin-orbital-lattice coupled states are accurately calculated. The dynamical JT stabilization comparable to or larger than Curie-Weiss constants indicates the persistence of vibronic dynamics in the crystals. The analysis of the local magnetic moment and response to the magnetic field reveals the reasons for the large increase in effective moment with temperature in Ba_2YMoO_6 and for the local symmetry breaking in Ba_2NaOsO_6.

II. ELECTRONIC AND VIBRONIC MODEL FOR d^1 SYSTEMS

The electronic structure of a d^1 metal ion at an octahedral site is described by the ligand field $\hat{H}_{\mathrm{LF}}$, spin-orbit interaction $\hat{H}_{\mathrm{SO}}$, and vibronic coupling $\hat{H}_{\mathrm{JT}}$:

$$\hat{H} = \hat{H}_{\mathrm{LF}} + \hat{H}_{\mathrm{SO}} + \hat{H}_0 + \hat{H}_{\mathrm{JT}} + \hat{H}_{\mathrm{Zee}}, \tag{1}$$

where $\hat{H}_0$ is the Hamiltonian for harmonic oscillation and $\hat{H}_{\mathrm{Zee}}$ is the Zeeman interaction in applied magnetic field $\boldsymbol{B}$. The typical energy scales of $\hat{H}_{\mathrm{LF}}$, $\hat{H}_{\mathrm{SO}}$, $\hat{H}_{\mathrm{JT}}$, and $\hat{H}_{\mathrm{Zee}}$ under $|\boldsymbol{B}| \approx 10$ T are several, 0.1, 0.01, and 10^{-4}–10^{-3} eV, respectively, and should be treated in this order.

The ligand field $\hat{H}_{\mathrm{LF}}$ splits the atomic d level into e_g and t_{2g}, the latter being stabilized in an octahedral environment [35]. Due to the large ligand-field splitting, the low-energy states are well described in the space of t_{2g}^1 electron configurations. Since the orbital angular momentum on sites $\hat{\boldsymbol{l}}$ is not quenched, the spin-orbit coupling is operative already in the first order [35,36]:

$$\hat{H}_{\mathrm{SO}} = \lambda_{\mathrm{SO}} \tilde{\boldsymbol{l}} \cdot \hat{\boldsymbol{s}}. \tag{2}$$

Here, $\lambda_{\mathrm{SO}} > 0$ is the spin-orbit coupling parameter, $\tilde{\boldsymbol{l}}$ is the $\tilde{l} = 1$ effective orbital angular momentum operator of the t_{2g} orbitals, and $\hat{\boldsymbol{s}}$ is the electron spin. $\tilde{\boldsymbol{l}}$ behaves as $-\hat{\boldsymbol{l}}_p$, where $\hat{\boldsymbol{l}}_p$ is the orbital angular momentum for p orbitals [35,36]. The spin-orbit coupling $\hat{H}_{\mathrm{SO}}$ splits the sixfold t_{2g}^1 configurations into Γ_7 ($J = \frac{1}{2}$) and Γ_8 ($J = \frac{3}{2}$) multiplets [37]. The latter is the ground state separated from the former by $\frac{3}{2}\lambda_{\mathrm{SO}}$.

Because of the unquenched orbital momentum, the magnetic moment on the metal sites becomes

$$\hat{\boldsymbol{m}} = -\mu_{\mathrm{B}}(\langle l \rangle \tilde{\boldsymbol{l}} + g_e \hat{\boldsymbol{s}}), \tag{3}$$

where μ_{B} is the Bohr magneton, $\langle l \rangle$ is the expectation value of $\hat{\boldsymbol{l}}$, and g_e is the electron's g factor. Since $\tilde{\boldsymbol{l}}$ is opposite to $\hat{\boldsymbol{l}}_p$, the orbital and spin contributions partially cancel each other

---

*naoya.iwahara@gmail.com

†liviu.chibotaru@gmail.com

2469-9950/2018/98(7)/075138(12)

TABLE I. Spin-orbit coupling parameter $\lambda_{\rm SO}$ (meV), orbital angular momenta $\langle l \rangle$, vibrational frequency ω_Λ (meV), and vibronic coupling parameters $v_{n\Lambda}^{\Lambda_1\cdots\Lambda_k}$ (a.u.). Here, (1) and (2) following $\langle l \rangle$ stand for post-HF and DFT values, respectively.

	Ba_2LiOsO_6	Ba_2NaOsO_6	Ba_2YMoO_6
$\lambda_{\rm SO}$	379.9	384.5	88.1
$\langle l \rangle$ (1)	0.772	0.779	0.859
$\langle l \rangle$ (2)	0.551	0.562	0.643
ω_E	99.10	100.94	100.50
ω_{T_2}	50.37	49.43	46.52
v_E	-3.2998×10^{-4}	-2.6436×10^{-4}	1.0199×10^{-4}
v_{T_2}	0.4963×10^{-4}	0.4945×10^{-4}	0.7334×10^{-4}
v_E^{EE}	-1.6604×10^{-5}	-1.2693×10^{-5}	0.0821×10^{-5}
$v_E^{T_2T_2}$	-0.0850×10^{-5}	-0.0842×10^{-5}	-0.0646×10^{-5}
$v_{T_2}^{T_2T_2}$	-0.0011×10^{-5}	-0.0006×10^{-5}	0.0002×10^{-5}
$v_{T_2}^{ET_2}$	-0.0388×10^{-5}	-0.0289×10^{-5}	0.0248×10^{-5}
$v_{A_1}^{EEE}$	0.1151×10^{-6}	0.1032×10^{-6}	0.0009×10^{-6}
v_E^{EEE}	2.7380×10^{-6}	2.0917×10^{-6}	0.0290×10^{-6}
$v_{A_1}^{EEEE}$	-0.3158×10^{-7}	-0.2011×10^{-7}	0.0112×10^{-7}
v_{1E}^{EEEE}	2.5417×10^{-7}	1.6786×10^{-7}	-0.0362×10^{-7}
v_{2E}^{EEEE}	0.6240×10^{-7}	0.4204×10^{-7}	-0.0004×10^{-7}

[35,36,38]. This cancellation is almost complete in the atomic limit, $\langle l \rangle = 1$, while it is not in crystals because of covalency effects ($\langle l \rangle < 1$).

The t_{2g} orbitals also couple to the e_g and t_{2g} lattice vibrations [39–41]:

$$\hat{H}_{\rm JT} = \sum_k \sum_{n\Lambda\lambda} \sum_{\Lambda_1,\Lambda_2\cdots\Lambda_k} \frac{1}{k!} v_{n\Lambda}^{\Lambda_1\Lambda_2\cdots\Lambda_k} \times \{\hat{Q}_{\Lambda_1} \otimes \hat{Q}_{\Lambda_2} \otimes \cdots \otimes \hat{Q}_{\Lambda_k}\}_{n\Lambda\lambda} \hat{\tau}_{\Lambda\lambda}. \tag{4}$$

Here, Λ (Λ_i) is e_g or t_{2g}, λ is its component, n distinguishes the repeated representation, $\hat{Q}_{\Lambda\lambda}$ is the (mass-weighted) normal coordinate, $\{\hat{Q}_{\Lambda_1} \otimes \hat{Q}_{\Lambda_2} \otimes \cdots \otimes \hat{Q}_{\Lambda_k}\}_{\Lambda\lambda}$ is the symmetrized product of coordinates, $v_{n\Lambda}^{\Lambda_1\Lambda_2\cdots\Lambda_k}$ is the kth order orbital vibronic coupling parameter, and $\hat{\tau}_{\Lambda\lambda}$ are the matrices of Clebsch-Gordan coefficients.

For the details of the model Hamiltonian, see Appendix A.

III. *AB INITIO* DERIVATION OF COUPLING PARAMETERS

The spin-orbit $\lambda_{\rm SO}$ and vibronic $v_{n\Lambda}^{\Lambda_1\cdots\Lambda_k}$ coupling parameters were derived from the cluster calculations with post-Hartree-Fock (HF) methods, while $\langle l \rangle$ were extracted by both (1) post-HF and (2) density functional theory (DFT) calculations (see Appendices B 1 and B 2). The obtained parameters are listed in Table I.

The vibronic coupling in Ba_2AOsO_6 is stronger than in Ba_2YMoO_6. Particularly, the nonlinear vibronic coupling to the e_g modes is about 10–100 times stronger in the former compounds. Moreover, the vibronic coupling parameters of Ba_2AOsO_6 differ from each other. The strength of the vibronic coupling is determined by the overlap between the t_{2g} orbital and the distribution of the vibronic operator. The former depends on the type of d orbital (4d or 5d) and also the environment such as the metal-oxygen bond length [42], resulting in different vibronic coupling parameters.

In all compounds, the expectation value of the orbital angular momentum $\langle l \rangle$ is reduced from unity due to the delocalization of the t_{2g} electron over ligands. As expected, the DFT values are smaller by 25%–30% than post-HF values since the latter underestimates metal-ligand covalency. The present DFT value of $\langle l \rangle$ for Ba_2NaOsO_6 is close to the previous calculation, 0.536 [17]. The spin-orbit coupling parameters $\lambda_{\rm SO}$ from the *ab initio* calculations are also in good agreement with previous calculations [16]. However, as in the case of $\langle l \rangle$, $\lambda_{\rm SO}$ may be overestimated by post-HF calculations. Since both $\langle l \rangle$ and $\lambda_{\rm SO}$ are mainly contributed by the d metal orbitals, the covalent reduction of the latter should be similar to the former.

IV. JAHN-TELLER EFFECT

A. Static Jahn-Teller deformation

The derived parameters show that the energy scales for the multiplet splitting and vibrational frequencies ω_Λ are comparable, particularly in the case of Ba_2YMoO_6. This makes relevant the pseudo-JT effect between the Γ_7 and Γ_8 multiplets, along with the JT effect in each of them. Indeed, the adiabatic potential-energy surfaces (APESs) along the JT distortion with and without pseudo-JT coupling show non-negligible differences: the APES of the $\Gamma_8 \otimes e_g$ JT model (gray circles) is modified (red squares) even in the case of Ba_2AOsO_6 with large $\lambda_{\rm SO}$ [Fig. 1(a)]. Thus, for an adequate description of the d^1 site, the consideration of the full $(\Gamma_7 \oplus \Gamma_8) \otimes (e_g \oplus t_{2g})$ JT coupling is essential. Figure 1(a) also shows the unexpectedly strong effect of nonlinear vibronic coupling: the positions of the minima and saddle point of the APESs within the linear model (blue circles) are inverted by nonlinear coupling (red squares).

The global minima and saddle points of the APESs were investigated as in the simpler case of the $\Gamma_8 \otimes (e_g \oplus t_{2g})$ JT problem [43] (for details, see [44]). The results are summarized in Table II. The static JT distortions for Ba_2AOsO_6 develop only along the e_g mode [Fig. 1(b)]. The JT stabilization energies $|U_{\rm min}|$ are 32.2 and 20.3 meV [45], and the energy barriers ΔU between the minima and the saddle points in the bottom of the APESs are only 10.9 and 6.3 meV for $A =$ Li and Na, respectively [for $A =$ Na see Fig. 1(a)]. In contrast, in Ba_2YMoO_6 the t_{2g} distortion is dominant [Fig. 1(c)]. The stabilization energy is only 4.8 meV [45], and the energy barrier at the trigonal point ($Q_{T_2\xi} = Q_{T_2\eta} = Q_{T_2\zeta}$) is about 0.7 meV.

In all materials, the largest shifts $\delta l_{\rm max}$ of the oxygen atom by the static JT deformation obtained were about 0.02 Å which is larger than the experimental resolution [46], which at a glance seems to be contradictory to the absence of the symmetry lowering in the structural data. However, because of the small warping of the trough ΔU, the dynamical Jahn-Teller effect [40,41], which causes the delocalization of the nuclear wave function over the trough, has to be fully taken into account.

B. Spin-orbital-lattice entangled states

The vibronic eigenstates of the $(\Gamma_7 \oplus \Gamma_8) \otimes (e_g \oplus t_{2g})$ JT system have a spin-orbital-lattice entangled form:

$$|\Psi_{\alpha\Lambda M}\rangle = \sum_{\Gamma=\Gamma_7,\Gamma_8} \sum_N |\Gamma N\rangle \otimes |\psi_{\Gamma N,\alpha\Lambda M}\rangle, \tag{5}$$

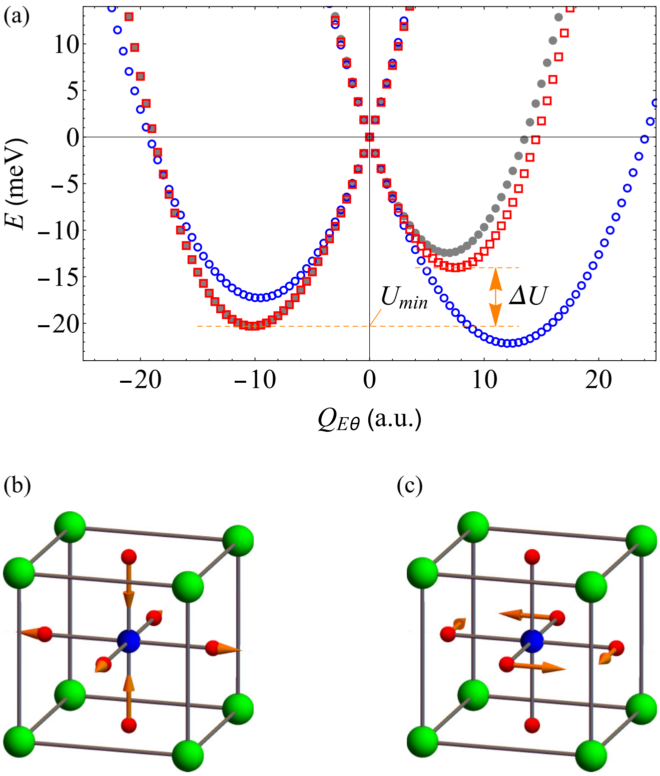

FIG. 1. (a) The APESs along the $e_g\theta$ distortion for Ba_2NaOsO_6 and JT distortions for (b) Os and (c) Mo compounds. In (a) the red squares and gray solid circles indicate the APESs with and without pseudo-JT coupling, respectively, and the blue open circles show the APESs of the linear JT model with pseudo-JT coupling. In (b) and (c), the orange arrows show the direction of the displacements of oxygen atoms at the minima of APESs.

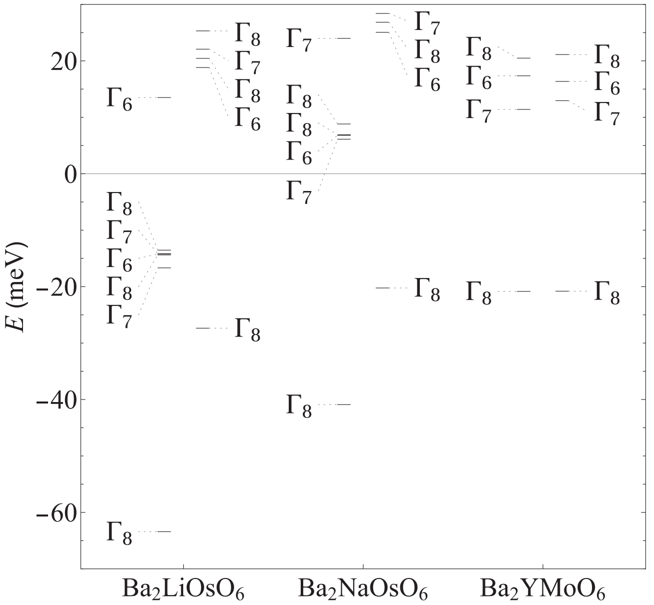

FIG. 2. Low-energy vibronic levels in double perovskites (meV). The left and right columns for each compound are the vibronic levels without and with nonlinear vibronic coupling. The ground energy without vibronic coupling is taken as the zero of the energy.

where α is the principal quantum number, $|\Gamma N\rangle$ is the multiplet state, and $|\psi_{\Gamma N,\alpha\Lambda M}\rangle$ is the nuclear part. The latter is expanded into the eigenstates of harmonic oscillators [47–49]. The vibronic states (5) were obtained by numerical diagonalization of the JT Hamiltonian (see Appendix B 4).

Figure 2 shows the vibronic levels without and with nonlinear vibronic coupling for each system. In Ba_2AOsO_6, the nonlinear vibronic coupling significantly destabilizes the linear vibronic states, which is explained by the rise in the minima of APESs and reduced magnitude of distortion at the minima [Fig. 1(a)] [50]. The resultant dynamical JT stabilizations are several times larger than the exchange interactions measured by Curie-Weiss constants Θ ($|\Theta| = 3.5$ meV for $A =$ Li and 0.9–2.8 meV for $A =$ Na [3,5]). Moreover, a rather weak intersite elastic interaction is expected because OsO_6 octahedrons have no common ligand atoms. The absence of a clear static cooperative JT effect (or orbital ordering) [5] is explained by its destruction by the unquenched JT dynamics, as is also the case in fullerides [29]. The presence of the JT dynamics means that the phase of the materials should be described in terms of the spin-orbital-lattice entangled states instead of spin or spin-orbit coupled states. Thus, for example, the low-temperature ordered phase [3] is not a simple magnetic one but that of spin-orbital-lattice entangled states. The impact of the difference on the physical properties will be discussed in Sec. V B.

TABLE II. The position of one of the minima (a.u.) and energy (meV). $\delta l_{\max}$ indicates the largest displacement of an oxygen atom under JT deformation, and $U_{\min}$ and ΔU are the JT stabilization energy and the energy barrier between the minima and saddle points, respectively (see Fig. 1).

	Ba_2LiOsO_6	Ba_2NaOsO_6	Ba_2YMoO_6
$Q_{E\theta}$	−12.29	−10.24	1.42
$Q_{T_2\zeta}$	0.00	0.00	11.46
$\delta l_{\max}$	0.022	0.018	0.018
$U_{\min}$	−32.22	−20.31	−4.84
ΔU	10.86	6.27	0.67

In the case of Ba_2YMoO_6, the energy gain by the JT dynamics amounts to as much as three times the static JT energy (as usual in the weak JT regime [40]). The dynamical JT stabilization is comparable in magnitude to the reported Θ ($|\Theta|$ ranges from 7.8 to 18.9 meV [4,7,8,11,13]; see Table III), implying a non-negligible contribution of the JT dynamics to the low-energy states, as discussed above. The first excited states arise at ∼30 meV above the ground one (Fig. 2), which should be put in relation to the excitation at ∼28 meV observed in inelastic neutron scattering measurements [9]. The presence of the JT dynamics does not contradict the temperature evolution of the infrared spectra which were attributed to the classical JT distortion at low temperature [13]. Indeed, a similar temperature dependence of infrared spectra of fullerides was explained on the basis of the dynamical JT effect [51].

V. MAGNETIC PROPERTIES

In the present systems, the vibronic states (5) inherit the paramagnetic properties from the spin-orbit multiplets.

TABLE III. Theoretical and experimental effective magnetic moments M_{eff} (in units of μ_{B}) and Curie-Weiss temperature Θ (meV). T (K) indicates the temperature for the simulation or measurements.

	M_{eff}	Θ	T	Method	Ref.
			High T		
Ba_2LiOsO_6	0.707		300	Theory (Vibronic)	This work
	0.733	-3.5	150–300	χ	[3]
Ba_2NaOsO_6	0.658		300	Theory (Vibronic)	This work
	0.677	-2.8	150–300	χ	[3]
	0.596–0.647	-0.9 to -1.3	75–200	χ	[5]
Ba_2YMoO_6	1.351		300	Theory (Vibronic)	This work
	1.231		300	Theory (Electronic)	This work
	1.34	-7.8	220–300	χ	[4]
	1.41	-13.8	150–300	χ	[7]
	1.72	-18.9	150–300	χ	[8]
	1.44	-12.3	160–390	χ	[11]
	1.52	-14.8	150–300	χ	[13]
			Low T		
Ba_2LiOsO_6	0.595		0	Theory (Vibronic)	This work
Ba_2NaOsO_6	0.569		0	Theory (Vibronic)	This work
	≈ 0.6		$\lesssim 10$	NMR	[18]
Ba_2YMoO_6	0.624		0	Theory (Vibronic)	This work
	0.462		0	Theory (Electronic)	This work
	0.53		<40	NMR	[8]
	0.59		<25	χ	[11]
	0.57		<25	χ	[13]

Particularly, because of the entanglement, the lattice degrees of freedom also become relevant to the magnetism. Below, two aspects are investigated.

A. Effective magnetic moment

The effective magnetic moment M_{eff} derived from the magnetic susceptibility χ at high temperature ($T > |\Theta|$) is expected to be close to that of a single d^1 site because the influence of intersite interactions in this case can be neglected. The temperature dependence of M_{eff} was calculated with (points) and without (lines) dynamical JT effect (Fig. 3). At $T = 0$ K, M_{eff} arises from only the Γ_8 vibronic states, and as temperature rises, it grows due to Van Vleck's second-order contribution [36,38]. The vibronic coupling influences M_{eff} in two ways: (i) JT coupling to Γ_8 multiplet modifies (often reduces) the matrix element of the electronic operator [49,52,53] and (ii) pseudo-JT coupling mixes the Γ_7 and Γ_8 multiplets. In the present case, the admixture of the Γ_7 multiplet with large magnetic moment leads to the enhancement of M_{eff}.

In the case of Ba_2AOsO_6, due to the strong $\hat{H}_{\mathrm{SO}}$, the Van Vleck contribution is small, and the temperature dependence of M_{eff} is weak [Fig. 3(a)]. The theoretical values with DFT $\langle l \rangle$ are in good agreement with the experimental data at both low and high temperatures: $M_{\mathrm{eff}} \approx 0.6\mu_{\mathrm{B}}$ at $T \approx 0$ K [18] and $0.60\mu_{\mathrm{B}}$–$0.68\mu_{\mathrm{B}}$ at high T [3,5] for Ba_2NaOsO_6 and $0.73\mu_{\mathrm{B}}$ at high T for Ba_2LiOsO_6 [3]. As is widely accepted [8,14,16,17], the d-p hybridization of Os and O atoms enlarges electronic M_{eff} (compare the data for the DFT-derived $\langle l \rangle$ and the atomic value). The JT dynamics slightly quenches the variation of M_{eff} [Fig. 3(a)].

On the other hand, in Ba_2YMoO_6, the pseudo-JT coupling plays a crucial role in enhancing M_{eff} [Fig. 3(b)]. At $T = 0$ K, M_{eff} amounts to $0.6\mu_{\mathrm{B}}$, which is in line with NMR of $0.53\mu_{\mathrm{B}}$ [8] and low-T susceptibility of $0.57\mu_{\mathrm{B}}$–$0.59\mu_{\mathrm{B}}$ [11,13,54], and it rapidly grows with T. Taking into account the covalency effect on both λ_{SO} and $\langle l \rangle$ (gray triangles), M_{eff} at $T \approx 300$ K reaches the experimental values ($1.3\mu_{\mathrm{B}}$–$1.5\mu_{\mathrm{B}}$ [4,7,11,13]).

B. Spin-orbital-lattice entanglement-driven magnetoelastic response

A peculiarity of the present systems is that the Zeeman splitting is accompanied by the variation of the $Q_{\Lambda\lambda}$ distribution in the ground Γ_8 vibronic state,

$$\rho_{\Gamma_8 M}(\boldsymbol{Q}) = \langle \Psi_{\Gamma_8 M} | \boldsymbol{Q} \rangle \langle \boldsymbol{Q} | \Psi_{\Gamma_8 M} \rangle, \tag{6}$$

where $\boldsymbol{Q}$ is a set of normal coordinates. Under $\boldsymbol{B} \parallel [001]$ the ground Γ_8 level splits as in the inset of Fig. 4(c). In the case of Os compounds, slight localization at the minima in the APESs is observed for $|\Psi_{\Gamma_8,\mp\frac{1}{2}}\rangle$ and around the saddle point for $|\Psi_{\Gamma_8,\mp\frac{3}{2}}\rangle$ [for the case of Ba_2NaOsO_6 see Figs. 4(a) and 4(b)]. Thus, with the increase in temperature, the center of the distribution ρ shifts from the minima of APESs to the symmetric point [Fig. 1(c); for the definition of ρ see Appendix B 6].

The temperature evolution of ρ must be related to the observation of the broken local point symmetry in Ba_2NaOsO_6 [18,19]. The expectation value of the JT distortion is reduced by the JT dynamics, and it is consistent with the expected small JT deformation in the NMR study as well as x-ray data [5]. Besides the applied field, the exchange interaction between d^1 centers enhances the Zeeman splitting in the presence of magnetic order, which would cause the reduction of the magnetic entropy to $k_{\mathrm{B}} \ln 2$ [5]. Thus, the ordering in Ba_2NaOsO_6 [18] is not a conventional orbital ordering with classical (static) JT

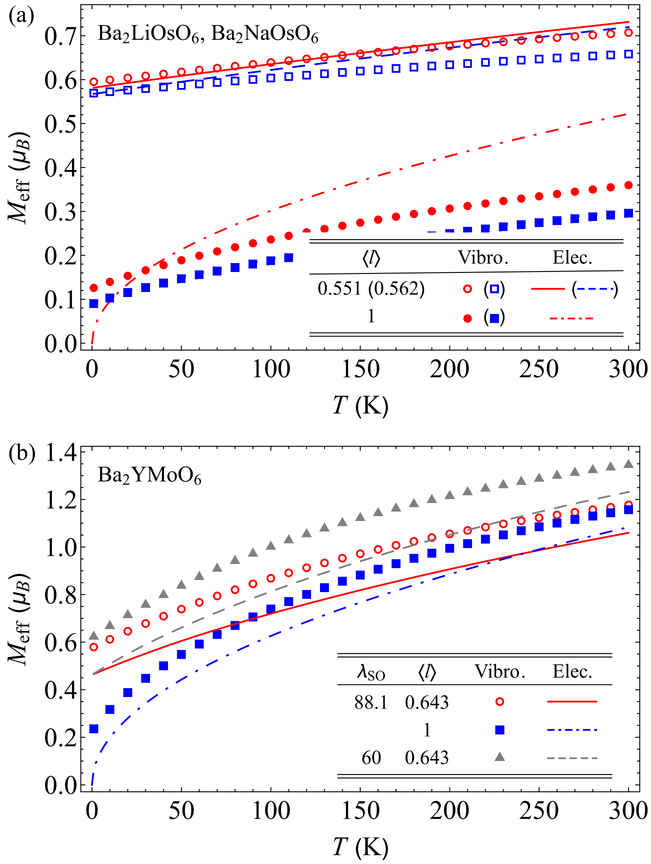

FIG. 3. Effective magnetic moments M_{eff} as a function of temperature for (a) Os and (b) Mo compounds. The meaning of the symbols and lines is given in the insets. "Vibro." and "Elec." stand for M_{eff} calculated for dynamical JT states and for pure electronic multiplet states, respectively, and $\langle l \rangle$ (also λ_{SO} for Mo system) is the value used for the simulation. (a) The red circles and solid and dot-dashed lines are for Ba_2LiOsO_6, and the blue squares and dashed line are for Ba_2NaOsO_6.

distortions but an ordering of spin-orbital-lattice entangled states.

In contrast to the Os compounds, in Ba_2YMoO_6 no magnetic order develops down to 50 mK [11]. Despite the stronger exchange interaction [4,7,8,11,13] than in Ba_2AOsO_6, the absence of the ordering hinders the large Zeeman splitting of vibronic levels, and hence, the dynamical JT effect develops as supported by neutron diffraction data [8] and sustains the magnetic entropy of $k_B \ln 4$ observed by muon spin resonance [7].

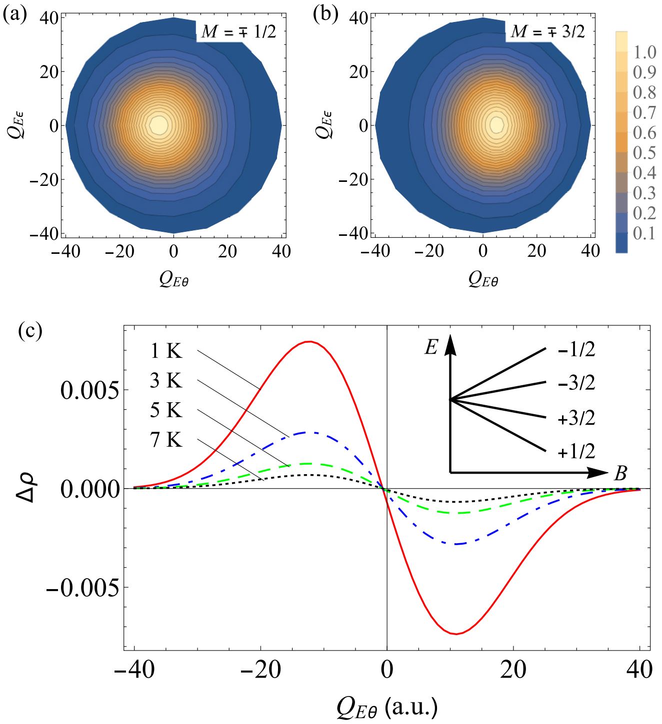

FIG. 4. (a) and (b) $\rho_{\Gamma_8 M}(Q_\theta, Q_\epsilon)$ for $M = \mp\frac{1}{2}$ and $\mp\frac{3}{2}$, respectively, and (c) the temperature evolution of the distribution of vibronic states for Ba_2NaOsO_6. In (a) and (b), the contour lines are drawn from zero with an increment of 1/20. In (c), the distribution with respect to the averaged one $\Delta\rho$ is shown under applied field of $|\boldsymbol{B}| = 15$ T. The inset shows the Zeeman splitting of the Γ_8 vibronic state. For the description of $\Delta\rho$, see Appendix B 6.

VI. CONCLUSION

The local spin-orbital-lattice entangled states of three cubic d^1 double perovskites were derived based on the first-principles approach. The gain of the energy of the ground coupled states is larger than (Ba_2AOsO_6) or comparable to (Ba_2YMoO_6) the corresponding Curie-Weiss constants, suggesting the presence of a dynamical JT effect in these materials. Due to the mixing with spin degrees of freedom, the vibronic states respond strongly to the magnetic field. Thus, the first excited vibronic level at ≈30 meV in Ba_2YMoO_6 suggests its relevance to the magnetic excitations measured in inelastic neutron scattering. In this compound, the vibronic coupling involving both Γ_8 and Γ_7 multiplets gives rise to the strong temperature dependence of the effective magnetic moment. In Ba_2AOsO_6, the entanglement gives rise to a magnetoelastic response where a small static component of the dynamical JT deformation accompanies the Zeeman splitting, which explains the breaking of local point symmetry.

The relevance of the spin-orbital-lattice entanglement is expected in other cubic d^1 [4,12,15] and d^2 double perovskites [55–59] and also in other types of cubic crystals such as $5d^1$ Ta chlorides retaining cubic symmetry down to low temperature [60]. For a complete understanding of the unconventional magnetic phases of the family of cubic double perovskites containing heavy transition metals, concomitant treatment of the vibronic and magnetic interactions is found to be crucial. The ordering of the spin-orbital-lattice entangled states would be a new direction towards unconventional multifunctional materials.

ACKNOWLEDGMENTS

N.I. is supported by a Japan Society for the Promotion of Science Overseas Research Fellowship. V.V. acknowledges the postdoctoral fellowship of the Fonds Wetenschappelijk Onderzoek-Vlaanderen (FWO, Flemish Science Foundation).

APPENDIX A: DERIVATION OF THE MODEL HAMILTONIAN

Here, the transformation of the model Hamiltonian for the t_{2g}^1 ion in an octahedral environment into the one in the basis of spin-orbit coupled states is shown in detail. In this appendix, the operators for the spin-orbital decoupled and coupled states are given by lowercase and uppercase letters, respectively, the subscript g of the representations is omitted in the equations for simplicity, and the coordinate axes of the d^1 system are chosen to correspond to C_4 axes.

According to the selection rule for the t_{2g} orbitals,

$$t_{2g} \otimes t_{2g} = a_{1g} \oplus e_g \oplus \{t_{1g}\} \oplus t_{2g}, \tag{A1}$$

the t_{2g} orbitals have unquenched orbital angular momenta (time-odd t_{1g} operator) and also couple to the a_{1g}, e_g, and t_{2g} vibrational modes (Fig. 5). In Eq. (A1), the curly brackets indicate that the representation is antisymmetric.

1. Electronic states

The presence of the unquenched orbital angular momenta indicates the spin-orbit coupling acts on t_{2g}^1 configurations in the first order of perturbation. Projecting the orbital angular momentum operator for the d orbitals into the space of t_{2g} orbitals, we obtain

$$\hat{\boldsymbol{l}} = \langle l \rangle \tilde{\boldsymbol{l}}, \tag{A2}$$

where the reduction of the orbital angular momentum by the covalency effect is included in $\langle l \rangle$ and the components of $\tilde{\boldsymbol{l}}$ are written as follows [35,36]:

$$\tilde{l}_x = \begin{pmatrix} 0 & 0 & 0 \\ 0 & 0 & i \\ 0 & -i & 0 \end{pmatrix}, \quad \tilde{l}_y = \begin{pmatrix} 0 & 0 & -i \\ 0 & 0 & 0 \\ i & 0 & 0 \end{pmatrix},$$
$$\tilde{l}_z = \begin{pmatrix} 0 & i & 0 \\ -i & 0 & 0 \\ 0 & 0 & 0 \end{pmatrix} \tag{A3}$$

in the order of the electronic basis $|t_2\xi\rangle$, $|t_2\eta\rangle$, $|t_2\zeta\rangle$. ξ, η, ζ indicate the basis of the t_{2g} representation and transform as yz, zx, xy, respectively, under the symmetry operation of the O_h group.

Due to the spin-orbit coupling, $\hat{h}_{\text{SO}} = \lambda_{\text{SO}} \tilde{\boldsymbol{l}} \cdot \hat{\boldsymbol{s}}$, t_{2g}^1 configurations split into spin-orbit multiplets [37]:

$$t_2 \otimes \Gamma_6 = \Gamma_7 \oplus \Gamma_8. \tag{A4}$$

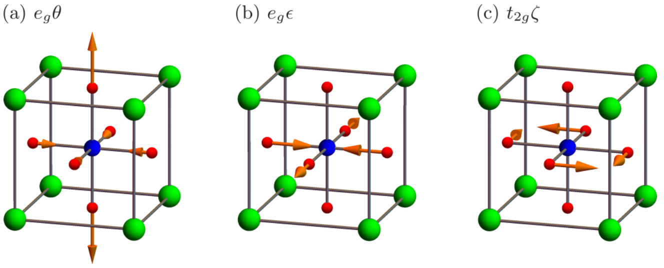

FIG. 5. Symmetrized mass-weighted normal vibrations. (a) $E_g\theta$, (b) $E_g\epsilon$, and (c) $T_{2g}\zeta$.

Γ_6 is the irreducible representation of the electron spin state. Since each representation appears only once on the right-hand side, the spin-orbit coupled states are determined by using Clebsch-Gordan coefficients as [37]

$$\begin{aligned}
\left|\Gamma_7, -\frac{1}{2}\right\rangle &= -\frac{i}{\sqrt{3}}|t_2\xi, \uparrow\rangle - \frac{1}{\sqrt{3}}|t_2\eta, \uparrow\rangle + \frac{i}{\sqrt{3}}|t_2\zeta, \downarrow\rangle, \\
\left|\Gamma_7, +\frac{1}{2}\right\rangle &= -\frac{i}{\sqrt{3}}|t_2\xi, \downarrow\rangle + \frac{1}{\sqrt{3}}|t_2\eta, \downarrow\rangle - \frac{i}{\sqrt{3}}|t_2\zeta, \uparrow\rangle, \\
\left|\Gamma_8, -\frac{3}{2}\right\rangle &= -\frac{i}{\sqrt{6}}|t_2\xi, \downarrow\rangle + \frac{1}{\sqrt{6}}|t_2\eta, \downarrow\rangle + i\sqrt{\frac{2}{3}}|t_2\zeta, \uparrow\rangle, \\
\left|\Gamma_8, -\frac{1}{2}\right\rangle &= \frac{i}{\sqrt{2}}|t_2\xi, \uparrow\rangle - \frac{1}{\sqrt{2}}|t_2\eta, \uparrow\rangle, \\
\left|\Gamma_8, +\frac{1}{2}\right\rangle &= -\frac{i}{\sqrt{2}}|t_2\xi, \downarrow\rangle - \frac{1}{\sqrt{2}}|t_2\eta, \downarrow\rangle, \\
\left|\Gamma_8, +\frac{3}{2}\right\rangle &= \frac{i}{\sqrt{6}}|t_2\xi, \uparrow\rangle + \frac{1}{\sqrt{6}}|t_2\eta, \uparrow\rangle + i\sqrt{\frac{2}{3}}|t_2\zeta, \downarrow\rangle.
\end{aligned} \tag{A5}$$

With the use of the spin-orbit coupled basis, Eq. (A5), the magnetic moment (3) in the Zeeman Hamiltonian, the matrix forms of the pseudo-orbital and spin angular momentum operators are given as

$$\hat{L}_x = \begin{pmatrix}
0 & -\frac{2}{3} & \frac{1}{3\sqrt{2}} & 0 & \frac{1}{\sqrt{6}} & 0 \\
-\frac{2}{3} & 0 & 0 & -\frac{1}{\sqrt{6}} & 0 & -\frac{1}{3\sqrt{2}} \\
\frac{1}{3\sqrt{2}} & 0 & 0 & \frac{1}{\sqrt{3}} & 0 & -\frac{2}{3} \\
0 & -\frac{1}{\sqrt{6}} & \frac{1}{\sqrt{3}} & 0 & 0 & 0 \\
\frac{1}{\sqrt{6}} & 0 & 0 & 0 & 0 & \frac{1}{\sqrt{3}} \\
0 & -\frac{1}{3\sqrt{2}} & -\frac{2}{3} & 0 & \frac{1}{\sqrt{3}} & 0
\end{pmatrix},$$

$$\hat{L}_y = \begin{pmatrix}
0 & -\frac{2i}{3} & \frac{i}{3\sqrt{2}} & 0 & -\frac{i}{\sqrt{6}} & 0 \\
\frac{2i}{3} & 0 & 0 & -\frac{i}{\sqrt{6}} & 0 & \frac{i}{3\sqrt{2}} \\
-\frac{i}{3\sqrt{2}} & 0 & 0 & \frac{i}{\sqrt{3}} & 0 & \frac{2i}{3} \\
0 & \frac{i}{\sqrt{6}} & -\frac{i}{\sqrt{3}} & 0 & 0 & 0 \\
\frac{i}{\sqrt{6}} & 0 & 0 & 0 & 0 & \frac{i}{\sqrt{3}} \\
0 & -\frac{i}{3\sqrt{2}} & -\frac{2i}{3} & 0 & -\frac{i}{\sqrt{3}} & 0
\end{pmatrix},$$

$$\hat{L}_z = \begin{pmatrix}
\frac{2}{3} & 0 & 0 & 0 & 0 & -\frac{\sqrt{2}}{3} \\
0 & -\frac{2}{3} & -\frac{\sqrt{2}}{3} & 0 & 0 & 0 \\
0 & -\frac{\sqrt{2}}{3} & -\frac{1}{3} & 0 & 0 & 0 \\
0 & 0 & 0 & -1 & 0 & 0 \\
0 & 0 & 0 & 0 & 1 & 0 \\
-\frac{\sqrt{2}}{3} & 0 & 0 & 0 & 0 & \frac{1}{3}
\end{pmatrix}, \tag{A6}$$

and

$$\hat{S}_x = \begin{pmatrix} 0 & -\frac{1}{6} & \frac{1}{3\sqrt{2}} & 0 & \frac{1}{\sqrt{6}} & 0 \\ -\frac{1}{6} & 0 & 0 & -\frac{1}{\sqrt{6}} & 0 & -\frac{1}{3\sqrt{2}} \\ \frac{1}{3\sqrt{2}} & 0 & 0 & -\frac{1}{2\sqrt{3}} & 0 & \frac{1}{3} \\ 0 & -\frac{1}{\sqrt{6}} & -\frac{1}{2\sqrt{3}} & 0 & 0 & 0 \\ \frac{1}{\sqrt{6}} & 0 & 0 & 0 & 0 & -\frac{1}{2\sqrt{3}} \\ 0 & -\frac{1}{3\sqrt{2}} & \frac{1}{3} & 0 & -\frac{1}{2\sqrt{3}} & 0 \end{pmatrix},$$

$$\hat{S}_y = \begin{pmatrix} 0 & -\frac{i}{6} & \frac{i}{3\sqrt{2}} & 0 & -\frac{i}{\sqrt{6}} & 0 \\ \frac{i}{6} & 0 & 0 & -\frac{i}{\sqrt{6}} & 0 & \frac{i}{3\sqrt{2}} \\ -\frac{i}{3\sqrt{2}} & 0 & 0 & -\frac{i}{2\sqrt{3}} & 0 & -\frac{i}{3} \\ 0 & \frac{i}{\sqrt{6}} & \frac{i}{2\sqrt{3}} & 0 & 0 & 0 \\ \frac{i}{\sqrt{6}} & 0 & 0 & 0 & 0 & -\frac{i}{2\sqrt{3}} \\ 0 & -\frac{i}{3\sqrt{2}} & \frac{i}{3} & 0 & \frac{i}{2\sqrt{3}} & 0 \end{pmatrix},$$

$$\hat{S}_z = \begin{pmatrix} \frac{1}{6} & 0 & 0 & 0 & 0 & -\frac{\sqrt{2}}{3} \\ 0 & -\frac{1}{6} & -\frac{\sqrt{2}}{3} & 0 & 0 & 0 \\ 0 & -\frac{\sqrt{2}}{3} & \frac{1}{6} & 0 & 0 & 0 \\ 0 & 0 & 0 & \frac{1}{2} & 0 & 0 \\ 0 & 0 & 0 & 0 & -\frac{1}{2} & 0 \\ -\frac{\sqrt{2}}{3} & 0 & 0 & 0 & 0 & -\frac{1}{6} \end{pmatrix}, \tag{A7}$$

respectively. The basis has the same order as Eq. (A5). The spin-orbit, $\hat{h}_{\mathrm{SO}} = \lambda_{\mathrm{SO}} \tilde{\boldsymbol{l}} \cdot \hat{\boldsymbol{s}}$, and Zeeman, $\hat{h}_{\mathrm{Zee}} = -\hat{\boldsymbol{m}} \cdot \boldsymbol{B}$, Hamiltonian matrices in the coupled basis are obtained by simply replacing $\tilde{\boldsymbol{l}}$ and $\hat{\boldsymbol{s}}$ by $\hat{\boldsymbol{L}}$ and $\hat{\boldsymbol{S}}$, respectively.

2. Vibronic coupling

The t_{2g} orbital couples to a_{1g}, e_g, and t_{2g} vibrations (A1). We take the O_h structure which is fully relaxed with respect to the a_g normal mode as a reference structure. The totally symmetric part contains harmonic and anharmonic potentials:

$$\begin{aligned} \hat{h}_{A_1} = & \sum_{\gamma=\theta,\epsilon} \frac{\omega_E^2}{2} \hat{Q}_{E\gamma}^2 + \sum_{\gamma=\xi,\eta,\zeta} \frac{\omega_{T_2}^2}{2} \hat{Q}_{T_2\gamma}^2 \\ & + \sum_{\gamma=\theta,\epsilon} \frac{v_{A_1}^{EEE}}{3!} \{\hat{Q}_E \otimes \hat{Q}_E \otimes \hat{Q}_E\}_{A_1} \\ & + \sum_{\gamma=\theta,\epsilon} \frac{v_{A_1}^{EEEE}}{4!} \{\hat{Q}_E \otimes \hat{Q}_E \otimes \hat{Q}_E \otimes \hat{Q}_E\}_{A_1}. \end{aligned} \tag{A8}$$

Here, ω_Γ is the frequency of the Γ mode ($\Gamma = E, T_2$). The symmetrized products are shown below. The bases of the e_g representation expressed by θ and ϵ transform as $(-x^2 - y^2 + 2z^2)/\sqrt{6}$ and $(x^2 - y^2)/\sqrt{2}$, respectively, under symmetry operations.

The vibronic couplings with the e_g and t_{2g} modes induce the Jahn-Teller effect. The linear term is given by

$$\hat{h}_{\mathrm{LJT}} = \sum_{\gamma=\theta,\epsilon} v_E \hat{Q}_{E\gamma} \hat{\tau}_{E\gamma} + \sum_{\gamma=\xi,\eta,\zeta} v_{T_2} \hat{Q}_{T_2\gamma} \hat{\tau}_{T_2\gamma}. \tag{A9}$$

Here, v_Γ are the linear orbital vibronic coupling parameters, and $\hat{\boldsymbol{\tau}}$ are matrices of Clebsch-Gordan coefficients:

$$\hat{\tau}_{E\theta} = \begin{pmatrix} -\frac{1}{2} & 0 & 0 \\ 0 & -\frac{1}{2} & 0 \\ 0 & 0 & 1 \end{pmatrix}, \quad \hat{\tau}_{E\epsilon} = \begin{pmatrix} \frac{\sqrt{3}}{2} & 0 & 0 \\ 0 & -\frac{\sqrt{3}}{2} & 0 \\ 0 & 0 & 0 \end{pmatrix},$$
$$\hat{\tau}_{T_2\xi} = \begin{pmatrix} 0 & 0 & 0 \\ 0 & 0 & \frac{1}{\sqrt{2}} \\ 0 & \frac{1}{\sqrt{2}} & 0 \end{pmatrix}, \quad \hat{\tau}_{T_2\eta} = \begin{pmatrix} 0 & 0 & \frac{1}{\sqrt{2}} \\ 0 & 0 & 0 \\ \frac{1}{\sqrt{2}} & 0 & 0 \end{pmatrix},$$
$$\hat{\tau}_{T_2\zeta} = \begin{pmatrix} 0 & \frac{1}{\sqrt{2}} & 0 \\ \frac{1}{\sqrt{2}} & 0 & 0 \\ 0 & 0 & 0 \end{pmatrix}. \tag{A10}$$

The phase factors of the Jahn-Teller active modes are chosen as shown in Fig. 5.

Transforming the electronic basis from the spin-orbital decoupled states into the coupled states (A5), $\hat{\boldsymbol{\tau}}$ in $\hat{h}_{\mathrm{LJT}}$ become

$$\hat{T}_{E\theta} = \begin{pmatrix} 0 & 0 & 0 & 0 & 0 & \frac{1}{\sqrt{2}} \\ 0 & 0 & -\frac{1}{\sqrt{2}} & 0 & 0 & 0 \\ 0 & -\frac{1}{\sqrt{2}} & \frac{1}{2} & 0 & 0 & 0 \\ 0 & 0 & 0 & -\frac{1}{2} & 0 & 0 \\ 0 & 0 & 0 & 0 & -\frac{1}{2} & 0 \\ \frac{1}{\sqrt{2}} & 0 & 0 & 0 & 0 & \frac{1}{2} \end{pmatrix},$$

$$\hat{T}_{E\epsilon} = \begin{pmatrix} 0 & 0 & 0 & -\frac{1}{\sqrt{2}} & 0 & 0 \\ 0 & 0 & 0 & 0 & \frac{1}{\sqrt{2}} & 0 \\ 0 & 0 & 0 & 0 & \frac{1}{2} & 0 \\ -\frac{1}{\sqrt{2}} & 0 & 0 & 0 & 0 & \frac{1}{2} \\ 0 & \frac{1}{\sqrt{2}} & \frac{1}{2} & 0 & 0 & 0 \\ 0 & 0 & 0 & \frac{1}{2} & 0 & 0 \end{pmatrix},$$

$$\hat{T}_{T_2\xi} = \begin{pmatrix} 0 & 0 & -\frac{i}{2} & 0 & \frac{i}{2\sqrt{3}} & 0 \\ 0 & 0 & 0 & -\frac{i}{2\sqrt{3}} & 0 & \frac{i}{2} \\ \frac{i}{2} & 0 & 0 & \frac{i}{\sqrt{6}} & 0 & 0 \\ 0 & \frac{i}{2\sqrt{3}} & -\frac{i}{\sqrt{6}} & 0 & 0 & 0 \\ -\frac{i}{2\sqrt{3}} & 0 & 0 & 0 & 0 & -\frac{i}{\sqrt{6}} \\ 0 & -\frac{i}{2} & 0 & 0 & \frac{i}{\sqrt{6}} & 0 \end{pmatrix},$$

$$\hat{T}_{T_2\eta} = \begin{pmatrix} 0 & 0 & -\frac{1}{2} & 0 & -\frac{1}{2\sqrt{3}} & 0 \\ 0 & 0 & 0 & -\frac{1}{2\sqrt{3}} & 0 & -\frac{1}{2} \\ -\frac{1}{2} & 0 & 0 & \frac{1}{\sqrt{6}} & 0 & 0 \\ 0 & -\frac{1}{2\sqrt{3}} & \frac{1}{\sqrt{6}} & 0 & 0 & 0 \\ -\frac{1}{2\sqrt{3}} & 0 & 0 & 0 & 0 & -\frac{1}{\sqrt{6}} \\ 0 & -\frac{1}{2} & 0 & 0 & -\frac{1}{\sqrt{6}} & 0 \end{pmatrix},$$

$$\hat{T}_{T_2\zeta} = \begin{pmatrix} 0 & 0 & 0 & -\frac{i}{\sqrt{3}} & 0 & 0 \\ 0 & 0 & 0 & 0 & -\frac{i}{\sqrt{3}} & 0 \\ 0 & 0 & 0 & 0 & -\frac{i}{\sqrt{6}} & 0 \\ \frac{i}{\sqrt{3}} & 0 & 0 & 0 & 0 & -\frac{i}{\sqrt{6}} \\ 0 & \frac{i}{\sqrt{3}} & \frac{i}{\sqrt{6}} & 0 & 0 & 0 \\ 0 & 0 & 0 & \frac{i}{\sqrt{6}} & 0 & 0 \end{pmatrix}. \tag{A11}$$

Replacing $\hat{\boldsymbol{\tau}}$ in $\hat{h}_{\mathrm{LJT}}$ with $\hat{\boldsymbol{T}}$, we obtain $\hat{H}_{\mathrm{LJT}}$.

The nonlinear vibronic Hamiltonian is derived in the same manner:

$$\begin{aligned} \hat{h}_{\mathrm{NLJT}} = &\sum_{\gamma=\theta,\epsilon} \frac{v_E^{EE}}{2!}\{\hat{Q}_E \otimes \hat{Q}_E\}_{E\gamma}\hat{\tau}_{E\gamma} \\ &+ \sum_{\gamma=\theta,\epsilon} \frac{v_E^{T_2T_2}}{2!}\{\hat{Q}_{T_2} \otimes \hat{Q}_{T_2}\}_{E\gamma}\hat{\tau}_{E\gamma} \\ &+ \sum_{\gamma=\xi,\eta,\zeta} \frac{v_{T_2}^{T_2T_2}}{2!}\{\hat{Q}_{T_2} \otimes \hat{Q}_{T_2}\}_{T_2\gamma}\hat{\tau}_{T_2\gamma} \\ &+ \sum_{\gamma=\xi,\eta,\zeta} \frac{v_{T_2}^{ET_2}}{2!}\{\hat{Q}_E \otimes \hat{Q}_{T_2}\}_{T_2\gamma}\hat{\tau}_{T_2\gamma} \\ &+ \sum_{\gamma=\theta,\epsilon} \frac{v_E^{EEE}}{3!}\{\hat{Q}_E \otimes \hat{Q}_E \otimes \hat{Q}_E\}_{E\gamma}\hat{\tau}_{E\gamma} \\ &+ \sum_{n=1,2}\sum_{\gamma=\theta,\epsilon} \frac{v_{nE}^{EEEE}}{4!}\{\hat{Q}_E \\ &\otimes \hat{Q}_E \otimes \hat{Q}_E \otimes \hat{Q}_E\}_{nE\gamma}\hat{\tau}_{E\gamma}. \end{aligned} \tag{A12}$$

Here, only the terms treated in this work are written. Using the same transformation as for $\hat{h}_{\mathrm{LJT}}$, we obtain $\hat{H}_{\mathrm{NLJT}}$.

The symmetrized products of the coordinates appearing in Eqs. (A8) and (A12) are calculated as follows. The symmetrized quadratic coordinates are, in general, calculated as

$$\begin{aligned} \{\hat{Q}_{\Lambda_1} \otimes \hat{Q}_{\Lambda_2}\}_{\Lambda\lambda} = &\sum_{\lambda_1\lambda_2} \hat{Q}_{\Lambda_1\lambda_1}\hat{Q}_{\Lambda_2\lambda_2} \\ &\times \langle \Lambda_1\lambda_1\Lambda_2\lambda_2|(\Lambda_1\Lambda_2)\Lambda\lambda\rangle. \end{aligned} \tag{A13}$$

Here, $\langle \Lambda_1\lambda_1\Lambda_2\lambda_2|(\Lambda_1\Lambda_2)\Lambda\lambda\rangle$ is Clebsch-Gordan coefficient tabulated in Ref. [37]. The explicit forms of the symmetrized products of interest here are

$$\begin{aligned} \{\hat{Q}_E \otimes \hat{Q}_E\}_A &= \frac{1}{\sqrt{2}}\left(\hat{Q}_{E\theta}^2 + \hat{Q}_{E\epsilon}^2\right), \\ \{\hat{Q}_{T_2} \otimes \hat{Q}_{T_2}\}_A &= \frac{1}{\sqrt{3}}\left(\hat{Q}_{T_2\xi}^2 + \hat{Q}_{T_2\eta}^2 + \hat{Q}_{T_2\zeta}^2\right), \\ \{\hat{Q}_E \otimes \hat{Q}_E\}_{E\theta} &= -\frac{1}{\sqrt{2}}\left(\hat{Q}_{E\theta}^2 - \hat{Q}_{E\epsilon}^2\right), \\ \{\hat{Q}_E \otimes \hat{Q}_E\}_{E\epsilon} &= \sqrt{2}\hat{Q}_{E\theta}\hat{Q}_{E\epsilon}, \\ \{\hat{Q}_{T_2} \otimes \hat{Q}_{T_2}\}_{E\theta} &= -\frac{1}{\sqrt{6}}\left(\hat{Q}_{T_2\xi}^2 + \hat{Q}_{T_2\eta}^2 - 2\hat{Q}_{T_2\zeta}^2\right), \\ \{\hat{Q}_{T_2} \otimes \hat{Q}_{T_2}\}_{E\epsilon} &= \frac{1}{\sqrt{2}}\left(\hat{Q}_{T_2\xi}^2 - \hat{Q}_{T_2\eta}^2\right), \\ \{\hat{Q}_{T_2} \otimes \hat{Q}_{T_2}\}_{T_2\xi} &= \sqrt{2}\hat{Q}_{T_2\eta}\hat{Q}_{T_2\zeta}, \\ \{\hat{Q}_{T_2} \otimes \hat{Q}_{T_2}\}_{T_2\eta} &= \sqrt{2}\hat{Q}_{T_2\zeta}\hat{Q}_{T_2\xi}, \\ \{\hat{Q}_{T_2} \otimes \hat{Q}_{T_2}\}_{T_2\zeta} &= \sqrt{2}\hat{Q}_{T_2\xi}\hat{Q}_{T_2\eta}, \\ \{\hat{Q}_E \otimes \hat{Q}_{T_2}\}_{T_2\xi} &= \left(-\frac{1}{2}\hat{Q}_{E\theta} + \frac{\sqrt{3}}{2}\hat{Q}_{E\epsilon}\right)\hat{Q}_{T_2\xi}, \\ \{\hat{Q}_E \otimes \hat{Q}_{T_2}\}_{T_2\eta} &= \left(-\frac{1}{2}\hat{Q}_{E\theta} - \frac{\sqrt{3}}{2}\hat{Q}_{E\epsilon}\right)\hat{Q}_{T_2\eta}, \\ \{\hat{Q}_E \otimes \hat{Q}_{T_2}\}_{T_2\zeta} &= \hat{Q}_{E\theta}\hat{Q}_{T_2\zeta} \end{aligned} \tag{A14}$$

for quadratic terms. The cubic products can be calculated by using Eq. (A13) twice. The cubic terms of interest are calculated as follows:

$$\begin{aligned} \{\hat{Q}_E \otimes \{\hat{Q}_E \otimes \hat{Q}_E\}_E\}_{A_1} &= \tfrac{1}{2}\left(-\hat{Q}_{E\theta}^3 + 3\hat{Q}_{E\theta}\hat{Q}_{E\epsilon}^2\right), \\ \{\hat{Q}_E \otimes \{\hat{Q}_E \otimes \hat{Q}_E\}_E\}_{E\theta} &= \tfrac{1}{2}\hat{Q}_{E\theta}\left(\hat{Q}_{E\theta}^2 + \hat{Q}_{E\epsilon}^2\right), \\ \{\hat{Q}_E \otimes \{\hat{Q}_E \otimes \hat{Q}_E\}_E\}_{E\theta} &= \tfrac{1}{2}\hat{Q}_{E\epsilon}\left(\hat{Q}_{E\theta}^2 + \hat{Q}_{E\epsilon}^2\right). \end{aligned} \tag{A15}$$

The fourth-order terms for the E mode are calculated as

$$\begin{aligned} \{\hat{Q}_E \otimes \hat{Q}_E \otimes \hat{Q}_E \otimes \hat{Q}_E\}_{A_1} &= \{\hat{Q}_E \otimes \hat{Q}_E\}_{A_1}^2 = \frac{1}{2}\left(\hat{Q}_{E\theta}^2 + \hat{Q}_{E\epsilon}^2\right)^2, \\ \{\hat{Q}_E \otimes \hat{Q}_E \otimes \hat{Q}_E \otimes \hat{Q}_E\}_{1E\theta} &= \{\hat{Q}_E \otimes \hat{Q}_E\}_{A_1}\{\hat{Q}_E \otimes \hat{Q}_E\}_{E\theta} = -\frac{1}{2}\left(\hat{Q}_{E\theta}^2 - \hat{Q}_{E\epsilon}^2\right)\left(\hat{Q}_{E\theta}^2 + \hat{Q}_{E\epsilon}^2\right), \\ \{\hat{Q}_E \otimes \hat{Q}_E \otimes \hat{Q}_E \otimes \hat{Q}_E\}_{1E\epsilon} &= \{\hat{Q}_E \otimes \hat{Q}_E\}_{A_1}\{\hat{Q}_E \otimes \hat{Q}_E\}_{E\epsilon} = \hat{Q}_{E\theta}\hat{Q}_{E\epsilon}\left(\hat{Q}_{E\theta}^2 + \hat{Q}_{E\epsilon}^2\right), \\ \{\hat{Q}_E \otimes \hat{Q}_E \otimes \hat{Q}_E \otimes \hat{Q}_E\}_{2E\theta} &= \{\{\hat{Q}_E \otimes \hat{Q}_E\}_E \otimes \{\hat{Q}_E \otimes \hat{Q}_E\}_E\}_{E\theta} = -\frac{1}{2\sqrt{2}}\left(\hat{Q}_{E\theta}^4 + \hat{Q}_{E\epsilon}^4 - 6\hat{Q}_{E\theta}^2\hat{Q}_{E\epsilon}^2\right), \\ \{\hat{Q}_E \otimes \hat{Q}_E \otimes \hat{Q}_E \otimes \hat{Q}_E\}_{2E\epsilon} &= \{\{\hat{Q}_E \otimes \hat{Q}_E\}_E \otimes \{\hat{Q}_E \otimes \hat{Q}_E\}_E\}_{E\epsilon} = -\sqrt{2}\left(\hat{Q}_{E\theta}^2 - \hat{Q}_{E\epsilon}^2\right)\hat{Q}_{E\theta}\hat{Q}_{E\epsilon}. \end{aligned} \tag{A16}$$

APPENDIX B: COMPUTATIONAL DETAILS

1. *Ab initio* method

The electronic and vibronic coupling parameters were derived from the cluster calculations with post-Hartree-Fock (HF) methods and $\langle l \rangle$ were extracted with density functional theory (DFT) calculations. The clusters were generated from the experimental crystal structures [3,8] retaining O_h symmetry. In the post-HF calculations, the d^1 metal ion and the nearest six oxygen atoms were treated *ab initio* with atomic-natural-orbital relativistic-correlation consistent-valence quadruple zeta polarization (ANO-RCC-VQZP) basis functions, and the surrounding 280 atoms were replaced by the *ab initio* embedding model potential [61]. The atomic bielectronic integrals were calculated using Cholesky decomposition with a threshold of $1\times10^{-9}\,E_h$. Inversion symmetry was employed in all calculations.

All *ab initio* calculations were carried out with MOLCAS 8.0 [62] and were of the complete-active-space self-consistent-field (CASSCF)/extended multistate complete-active-space second-order perturbation theory (XMS-CASPT2) [63,64]/ spin-orbit restricted-active-space state interaction (SO-RASSI) type. The active space of all CASSCF calculations included seven electrons in six orbitals. Three orbitals are $4d$ or $5d$ orbitals, and the other three orbitals are of the ligand π type. Three roots were optimized at the CASSCF level, and then XMS-CASPT2 was carried out for the three roots from CASSCF. In XMS-CASPT2 calculations, the ionization potential electron affinity (IPEA) shift was set to zero, while the imaginary (IMAG) shift was set to 0.1. SO-RASSI calculations mixed the roots obtained from XMS-CASPT2 by spin-orbit coupling. The scalar relativistic effects were included in the basis set.

2. DFT method

The clusters for the DFT calculations contain 89 atoms which are treated explicitly with the default 2 triple zeta valence plus polarization (def2-TZVP) basis set and default 2 J auxiliary basis (def2/J) auxiliary basis sets. DFT calculations were done with the Becke three-parameter Lee-Yang-Parr (B3LYP) hybrid functional with the Resolution of the identity approximation for the Coulomb energy (J) and numerical chain-of-sphere integration for the Hartree-Fock exchange integrals (RIJCOSX) approximation. The basis function contains the scalar relativistic effects. For the DFT calculations, ORCA 4.0.0.2 [65] was used. For the SCF, condition TIGHTSCF is used. The grid for density was GRID5.

3. Calculations of electronic and vibronic coupling parameters

The spin-orbit coupling parameters $\lambda_{\rm SO}$ were obtained from the *ab initio* multiplet levels, $E_{\Gamma_7} - E_{\Gamma_8} = \frac{3}{2}\lambda_{\rm SO}$. The expectation values of orbital angular momentum $\langle l \rangle$ were calculated by using *ab initio* or DFT wave functions at the O_h structure. In the latter case, the orbital angular momentum matrices in the atomic orbital basis were calculated using MOLPRO 2012.1 [66]. The frequencies and vibronic parameters were derived by fitting the *ab initio* ${}^2T_{2g}$ adiabatic potential energy surface (APES) to the $t_{2g} \otimes (e_g \oplus t_{2g})$ model vibronic Hamiltonian [44]. The step of deformation is $\Delta Q = 0.5$ a.u. The units of the kth-order vibronic coupling parameter are $E_h/(m_e a_0^2)^{k/2}$, where E_h is Hartree, m_e is the electron mass, and a_0 is the Bohr radius.

4. Numerical diagonalization of the vibronic Hamiltonian

The $(\Gamma_7 \oplus \Gamma_8) \otimes (e_g \oplus t_{2g})$ JT Hamiltonians for the d^1 systems were numerically diagonalized with the derived parameters. The nuclear part of the vibronic state [Eq. (5)] is expressed as

$$|\psi_{\Gamma M,\alpha\Lambda\lambda}\rangle = \sum_{n_\theta,n_\epsilon,n_\xi,n_\eta,n_\zeta} |\boldsymbol{n}\rangle \psi_{\Gamma M\boldsymbol{n},\alpha\Lambda\lambda}, \tag{B1}$$

where $|\boldsymbol{n}\rangle = |n_\theta, n_\epsilon, n_\xi, n_\eta, n_\zeta\rangle$ $(n_\gamma \geqslant 0)$ are the eigenstates of $\hat{H}_0$ and the coefficient $\psi_{\Gamma M\boldsymbol{n},\alpha\Lambda\lambda}$ is defined by $\langle \boldsymbol{n} | \psi_{\Gamma M,\alpha\Lambda\lambda}\rangle$. The vibronic bases $|\Gamma\gamma\rangle \otimes |\boldsymbol{n}\rangle$ are truncated as

$$0 \leqslant \sum_\gamma n_\gamma \leqslant 9. \tag{B2}$$

The diagonalization of the dynamical JT Hamiltonian matrix was done in two steps. First, the linear JT Hamiltonian matrices,

$$\hat{H}^{(1)} = \hat{H}_{\rm SO} + \sum_{\Gamma\gamma} \frac{\hat{P}_{\Gamma\gamma}^2}{2} + \hat{H}_{A_1} + \hat{H}_{\rm LJT}, \tag{B3}$$

were diagonalized using LAPACK (ZHEEV). Then, using the lowest 1000 linear vibronic states as the basis, the nonlinear JT Hamiltonian matrices,

$$\hat{H}^{(2)} = \hat{H}^{(1)} + \hat{H}_{\rm NLJT}, \tag{B4}$$

were calculated and diagonalized.

5. Effective magnetic moment

The effective magnetic moments were calculated within pure electronic and vibronic models. The model Hamiltonians for these two cases are $\hat{H}_{\rm SO} + \hat{H}_{\rm Zee}$ and $\hat{H}^{(2)} + \hat{H}_{\rm Zee}$, respectively, where $\hat{H}^{(2)}$ corresponds to Eq. (B4). The magnetic field $\boldsymbol{B}$ was applied along the z axis, $\boldsymbol{B} = (0,0,B)$. The magnetic moments were calculated by

$$M_{\rm eff} = \sqrt{3k_{\rm B}T\chi(T)}, \tag{B5}$$

where $\chi(T)$ is the magnetic susceptibility, $\chi(T) = \beta^{-1}\partial^2 \ln Z(T,B)/\partial B^2|_{B\to 0}$, $\beta = 1/(k_{\rm B}T)$, and $Z(T,B)$ is the distribution function. In both cases, Van Vleck's contribution is directly included in the energy levels.

6. Distribution of vibronic states under Zeeman splitting

At low enough temperature that only the ground Γ_8 vibronic levels are occupied, the spatial distribution of the vibronic state is calculated as

$$\rho(\boldsymbol{Q},\boldsymbol{B},T) = \frac{\sum_M \rho_{\Gamma_8 M}(\boldsymbol{Q}) e^{-E_{\Gamma_8 M}(\boldsymbol{B})\beta}}{\sum_M e^{-E_{\Gamma_8 M}(\boldsymbol{B})\beta}}, \tag{B6}$$

where the sum is over the ground Γ_8 vibronic states and $E_{\Gamma_8 M}(\boldsymbol{B})$ is the Zeeman split vibronic level. The difference of the distribution $\Delta\rho$ in Fig. 1(c) is defined by

$$\Delta\rho(\boldsymbol{Q},\boldsymbol{B},T) = \rho(\boldsymbol{Q},\boldsymbol{B},T) - \bar{\rho}(\boldsymbol{Q}), \tag{B7}$$

where $\bar{\rho}$ is the averaged density over the ground vibronic states M, $\bar{\rho} = \sum_M \rho_{\Gamma_8 M}/4$.

[1] W. Witczak-Krempa, G. Chen, Y. B. Kim, and L. Balents, Correlated quantum phenomena in the strong spin-orbit regime, Annu. Rev. Condens. Matter Phys. **5**, 57 (2014).

[2] J. G. Rau, E. K.-H. Lee, and H.-Y. Kee, Spin-orbit physics giving rise to novel phases in correlated systems: Iridates and related materials, Annu. Rev. Condens. Matter Phys. **7**, 195 (2016).

[3] K. E. Stitzer, M. D. Smith, and H.-C. zur Loye, Crystal growth of Ba_2MOsO_6 (M = Li, Na) from reactive hydroxide fluxes, Solid State Sci. **4**, 311 (2002).

[4] E. J. Cussen, D. R. Lynham, and J. Rogers, Magnetic order arising from structural distortion: Structure and magnetic properties of Ba_2LnMoO_6, Chem. Mater. **18**, 2855 (2006).

[5] A. S. Erickson, S. Misra, G. J. Miller, R. R. Gupta, Z. Schlesinger, W. A. Harrison, J. M. Kim, and I. R. Fisher, Ferromagnetism in the Mott Insulator Ba_2NaOsO_6, Phys. Rev. Lett. **99**, 016404 (2007).

[6] H. J. Xiang and M.-H. Whangbo, Cooperative effect of electron correlation and spin-orbit coupling on the electronic and magnetic properties of Ba_2NaOsO_6, Phys. Rev. B **75**, 052407 (2007).

[7] M. A. de Vries, A. C. Mclaughlin, and J.-W. G. Bos, Valence Bond Glass on an fcc Lattice in the Double Perovskite Ba_2YMoO_6, Phys. Rev. Lett. **104**, 177202 (2010).

[8] T. Aharen, J. E. Greedan, C. A. Bridges, A. A. Aczel, J. Rodriguez, G. MacDougall, G. M. Luke, T. Imai, V. K. Michaelis, S. Kroeker, H. Zhou, C. R. Wiebe, and L. M. D. Cranswick, Magnetic properties of the geometrically frustrated $S = \frac{1}{2}$ antiferromagnets, La_2LiMoO_6 and Ba_2YMoO_6, with the B-site ordered double perovskite structure: Evidence for a collective spin-singlet ground state, Phys. Rev. B **81**, 224409 (2010).

[9] J. P. Carlo, J. P. Clancy, T. Aharen, Z. Yamani, J. P. C. Ruff, J. J. Wagman, G. J. Van Gastel, H. M. L. Noad, G. E. Granroth, J. E. Greedan, H. A. Dabkowska, and B. D. Gaulin, Triplet and in-gap magnetic states in the ground state of the quantum frustrated fcc antiferromagnet Ba_2YMoO_6, Phys. Rev. B **84**, 100404(R) (2011).

[10] A. J. Steele, P. J. Baker, T. Lancaster, F. L. Pratt, I. Franke, S. Ghannadzadeh, P. A. Goddard, W. Hayes, D. Prabhakaran, and S. J. Blundell, Low-moment magnetism in the double perovskites Ba_2MOsO_6 (M = Li, Na), Phys. Rev. B **84**, 144416 (2011).

[11] M. A. de Vries, J. O. Piatek, M. Misek, J. S. Lord, H. M. Rønnow, and J.-W. G. Bos, Low-temperature spin dynamics of a valence bond glass in Ba_2YMoO_6, New J. Phys. **15**, 043024 (2013).

[12] F. C. Coomer and E. J. Cussen, Structural and magnetic properties of Ba_2LuMoO_6: A valence bond glass, J. Phys.: Condens. Matter **25**, 082202 (2013).

[13] Z. Qu, Y. Zou, S. Zhang, L. Ling, L. Zhang, and Y. Zhang, Spin-phonon coupling probed by infrared transmission spectroscopy in the double perovskite Ba_2YMoO_6, J. Appl. Phys. **113**, 17E137 (2013).

[14] S. Gangopadhyay and W. E. Pickett, Spin-orbit coupling, strong correlation, and insulator-metal transitions: The $J_{eff} = \frac{3}{2}$ ferromagnetic Dirac-Mott insulator Ba_2NaOsO_6, Phys. Rev. B **91**, 045133 (2015).

[15] C. A. Marjerrison, C. M. Thompson, G. Sala, D. D. Maharaj, E. Kermarrec, Y. Cai, A. M. Hallas, M. N. Wilson, T. J. S. Munsie, G. E. Granroth, R. Flacau, J. E. Greedan, B. D. Gaulin, and G. M. Luke, Cubic Re^{6+} ($5d^1$) double perovskites, Ba_2MgReO_6, Ba_2ZnReO_6, and $Ba_2Y_{2/3}ReO_6$: Magnetism, heat capacity, μSR, and neutron scattering studies and comparison with theory, Inorg. Chem. **55**, 10701 (2016).

[16] L. Xu, N. A Bogdanov, A. Princep, P. Fulde, J. van den Brink, and L. Hozoi, Covalency and vibronic couplings make a nonmagnetic $j = 3/2$ ion magnetic, npj Quantum Mater. **1**, 16029 (2016).

[17] K.-H. Ahn, K. Pajskr, K.-W. Lee, and J. Kuneš, Calculated g-factors of $5d$ double perovskites Ba_2NaOsO_6 and Ba_2YOsO_6, Phys. Rev. B **95**, 064416 (2017).

[18] L. Lu, M. Song, W. Liu, A. P. Reyes, P. Kuhns, H. O. Lee, I. R. Fisher, and V. F. Mitrović, Magnetism and local symmetry breaking in a Mott insulator with strong spin orbit interactions, Nat. Commun. **8**, 14407 (2017).

[19] W. Liu, R. Cong, A. P. Reyes, I. R. Fisher, and V. F. Mitrović, Nature of lattice distortions in the cubic double perovskite Ba_2NaOsO_6, Phys. Rev. B **97**, 224103 (2018).

[20] G. Chen, R. Pereira, and L. Balents, Exotic phases induced by strong spin-orbit coupling in ordered double perovskites, Phys. Rev. B **82**, 174440 (2010).

[21] T. Dodds, T.-P. Choy, and Y. B. Kim, Interplay between lattice distortion and spin-orbit coupling in double perovskites, Phys. Rev. B **84**, 104439 (2011).

[22] H. Ishizuka and L. Balents, Magnetism in $S = \frac{1}{2}$ double perovskites with strong spin-orbit interactions, Phys. Rev. B **90**, 184422 (2014).

[23] W. M. H. Natori, E. C. Andrade, E. Miranda, and R. G. Pereira, Chiral Spin-Orbital Liquids with Nodal Lines, Phys. Rev. Lett. **117**, 017204 (2016).

[24] W. M. H. Natori, M. Daghofer, and R. G. Pereira, Dynamics of a $j = \frac{3}{2}$ quantum spin liquid, Phys. Rev. B **96**, 125109 (2017).

[25] J. Romhányi, L. Balents, and G. Jackeli, Spin-Orbit Dimers and Noncollinear Phases in d^1 Cubic Double Perovskites, Phys. Rev. Lett. **118**, 217202 (2017).

[26] C. Svoboda, M. Randeria, and N. Trivedi, Orbital and spin order in spin-orbit coupled d^1 and d^2 double perovskites, arXiv:1702.03199.

[27] H. A. Jahn, Stability of polyatomic molecules in degenerate electronic states. II. spin degeneracy, Proc. R. Soc. London, Ser. A **164**, 117 (1938).

[28] L. F. Chibotaru, Spin-Vibronic Superexchange in Mott-Hubbard Fullerides, Phys. Rev. Lett. **94**, 186405 (2005).

[29] N. Iwahara and L. F. Chibotaru, Dynamical Jahn-Teller Effect and Antiferromagnetism in Cs_3C_{60}, Phys. Rev. Lett. **111**, 056401 (2013).

[30] N. Iwahara and L. F. Chibotaru, Dynamical Jahn-Teller instability in metallic fullerides, Phys. Rev. B **91**, 035109 (2015).

[31] A. Krimmel, M. Mücksch, V. Tsurkan, M. M. Koza, H. Mutka, and A. Loidl, Vibronic and Magnetic Excitations in the Spin-Orbital Liquid State of $FeSc_2S_4$, Phys. Rev. Lett. **94**, 237402 (2005).

[32] S. Nakatsuji, K. Kuga, K. Kimura, R. Satake, N. Katayama, E. Nishibori, H. Sawa, R. Ishii, M. Hagiwara, F. Bridges, T. U. Ito, W. Higemoto, Y. Karaki, M. Halim, A. A. Nugroho, J. A. Rodriguez-Rivera, M. A. Green, and C. Broholm, Spin-orbital short-range order on a honeycomb-based lattice, Science **336**, 559 (2012).

[33] K. Kamazawa, M. Ishikado, S. Ohira-Kawamura, Y. Kawakita, K. Kakurai, K. Nakajima, and M. Sato, Interaction of spin-

orbital-lattice degrees of freedom: Vibronic state of the corner-sharing-tetrahedral frustrated spin system $HoBaFe_4O_7$ by dynamical Jahn-Teller effect, Phys. Rev. B **95**, 104413 (2017).

[34] R. Nirmala, K.-H. Jang, H. Sim, H. Cho, J. Lee, N.-G. Yang, S. Lee, R. M. Ibberson, K. Kakurai, M. Matsuda, S.-W. Cheong, V. V. Gapontsev, S. V. Streltsov, and J.-G. Park, Spin glass behavior in frustrated quantum spin system $CuAl_2O_4$ with a possible orbital liquid state, J. Phys.: Condens. Matter **29**, 13LT01 (2017).

[35] S. Sugano, Y. Tanabe, and H. Kamimura, *Multiplets of Transition-Metal Ions in Crystals* (Academic Press, New York, 1970).

[36] M. Kotani, Properties of d-electrons in complex salts. part I paramagnetism of complex salts, Prog. Theor. Phys. Suppl. **14**, 1 (1960).

[37] G. F. Koster, J. O. Dimmock, R. G. Wheeler, and H. Statz, *Properties of the Thirty-Two Point Groups* (MIT Press, Cambridge, MA, 1963).

[38] M. Kotani, On the magnetic moment of complex ions. (I), J. Phys. Soc. Jpn. **4**, 293 (1949).

[39] H. A. Jahn and E. Teller, Stability of polyatomic molecules in degenerate electronic states - I—Orbital degeneracy, Proc. R. Soc. London, Ser. A **161**, 220 (1937).

[40] I. B. Bersuker and V. Z. Polinger, *Vibronic Interactions in Molecules and Crystals* (Springer, Berlin, 1989).

[41] M. D. Kaplan and B. G. Vekhter, *Cooperative Phenomena in Jahn-Teller Crystals* (Plenum, New York, 1995).

[42] The Os-O distance in Ba_2LiOsO_6 is longer by 0.019 Å than that in Ba_2NaOsO_6.

[43] A. D. Liehr, Topological aspects of the conformational stability problem. Part I. Degenerate electronic states, J. Phys. Chem. **67**, 389 (1963).

[44] See Supplemental Material at http://link.aps.org/supplemental/10.1103/PhysRevB.98.075138 for the fitting of the APESs, the analysis of the static JT effect, and the vibronic levels.

[45] The present static JT stabilization energies are 1.5–3 times larger for Ba_2AOsO_6 and 10 times smaller for Ba_2YMoO_6 than the previous *ab initio* values obtained by the z-axis-only compression (10, 15, and 40 meV, respectively) [16]. There are two reasons for the discrepancy. (i) According to Fig. 2(b) in Ref. [16], the z-axis-only compression is a linear combination of a_{1g} and $e_g\theta$ modes. Since the experimental crystal structure is not fully relaxed in the sense of *ab initio* treatment, the contribution from the a_{1g} mode is included in the stabilization energy after the e_g mode. (ii) Relatively large numerical noise might modify the calculated vibronic coupling parameters due to the large deviation of the *ab initio* energy from their fitting curve (Fig. 2(c) in Ref. [16]).

[46] The resolution of the neutron scattering measurement of Ba_2YMoO_6 at 2.7 K is 0.2% of the lattice constant ($\approx$0.0167 Å) and that of the room-temperature x-ray scattering data is half of it [8]. In the NMR measurement, the distortion of Ba_2NaOsO_6 is expected to be between 0.002 and 0.066 Å [18].

[47] O. Kahn and S. F. A. Kettle, Influence du couplage vibronique sur le paramagnétisme d'un complexe cubique dans l'état électronique $^2T_2$, Theor. Chim. Acta **27**, 187 (1972).

[48] O. Kahn and S. F. A. Kettle, Vibronic coupling in cubic complexes, Mol. Phys. **29**, 61 (1975).

[49] N. Iwahara, V. Vieru, L. Ungur, and L. F. Chibotaru, Zeeman interaction and Jahn-Teller effect in the Γ_8 multiplet, Phys. Rev. B **96**, 064416 (2017).

[50] The reduction of the magnitude of JT distortion leads to the mixing of the excited linear vibronic states into the ground one. The ground Γ_8 states mainly consist of the ground linear Γ_8 vibronic states (87.2% for Ba_2LiOsO_6 and 93.5% for Ba_2NaOsO_6) and the excited ones involving two to four vibrational excitations at 46.9 and 78.1 meV, respectively (9.8% and 5.2%).

[51] Y. Matsuda, N. Iwahara, K. Tanigaki, and L. F. Chibotaru, Manifestation of vibronic dynamics in infrared spectra of Mott insulating fullerides, arXiv:1805.07753.

[52] M. S. Child and H. C. Longuet-Higgins, Studies of the Jahn-Teller effect III. The rotational and vibrational spectra of symmetric-top molecules in electronically degenerate states, Philos. Trans. R. Soc. London, Ser. A **254**, 259 (1961).

[53] F. S. Ham, Effect of linear jahn-teller coupling on paramagnetic resonance in a ^2E state, Phys. Rev. **166**, 307 (1968).

[54] NMR probes local properties, whereas the magnetic susceptibility reflects the macroscopic properties. Thus, the effect of the surroundings might be included in the low-T values from χ.

[55] K. Yamamura, M. Wakeshima, and Y. Hinatsu, Structural phase transition and magnetic properties of double perovskites Ba_2CaMO_6 (M = W, Re, Os), J. Solid State Chem. **179**, 605 (2006).

[56] T. Aharen, J. E. Greedan, C. A. Bridges, A. A. Aczel, J. Rodriguez, G. MacDougall, G. M. Luke, V. K. Michaelis, S. Kroeker, C. R. Wiebe, H. Zhou, and L. M. D. Cranswick, Structure and magnetic properties of the $S = 1$ geometrically frustrated double perovskites La_2LiReO_6 and Ba_2YReO_6, Phys. Rev. B **81**, 064436 (2010).

[57] C. M. Thompson, J. P. Carlo, R. Flacau, T. Aharen, I. A. Leahy, J. R. Pollichemi, T. J. S. Munsie, T. Medina, G. M. Luke, J. Munevar, S. Cheung, T. Goko, Y. J. Uemura, and J. E. Greedan, Long-range magnetic order in the $5d^2$ double perovskite Ba_2CaOsO_6: Comparison with spin-disordered Ba_2YReO_6, J. Phys.: Condens. Matter **26**, 306003 (2014).

[58] C. A. Marjerrison, C. M. Thompson, A. Z. Sharma, A. M. Hallas, M. N. Wilson, T. J. S. Munsie, R. Flacau, C. R. Wiebe, B. D. Gaulin, G. M. Luke, and J. E. Greedan, Magnetic ground states in the three $Os^{6+}(5d^2)$ double perovskites Ba_2MOsO_6(M = Mg, Zn, and Cd) from Néel order to its suppression, Phys. Rev. B **94**, 134429 (2016).

[59] H. L. Feng, S. Calder, M. P. Ghimire, Y.-H. Yuan, Y. Shirako, Y. Tsujimoto, Y. Matsushita, Z. Hu, C.-Y. Kuo, L. H. Tjeng, T.-W. Pi, Y.-L. Soo, J. He, M. Tanaka, Y. Katsuya, M. Richter, and K. Yamaura, Ba_2NiOsO_6: A Dirac-Mott insulator with ferromagnetism near 100 K, Phys. Rev. B **94**, 235158 (2016).

[60] H. Ishikawa, T. Takayama, R. K. Kremer, J. Nuss, R. Dinnebier, K. Kitagawa, K. Ishii, and H. Takagi, Ordering of hidden pseudo-dipolar moments in spin-orbital entangled $5d^1$ Ta chlorides, arXiv:1807.08311.

[61] L. Seijo and Z. Barandiarán, Computational Modelling of the Magnetic Properties of Lanthanide Compounds, in *Computational Chemistry: Reviews of Current Trends*, edited by J. Leszczynski (World Scientific, Singapore, 1999), Vol. 4, pp. 55–152.

[62] F. Aquilante, J. Autschbach, R. K. Carlson, L. F. Chibotaru, M. G. Delcey, L. De Vico, I. Fdez. Galván, N. Ferré, L. M. Frutos, L. Gagliardi, M. Garavelli, A. Giussani, C. E. Hoyer, G. Li Manni, H. Lischka, D. Ma, P.-Å. Malmqvist, T. Müller, A. Nenov, M. Olivucci, T. B. Pedersen, D. Peng, F. Plasser, B. Pritchard, M. Reiher, I. Rivalta, I. Schapiro, J. Segarra-Martí, M. Stenrup,

D. G. Truhlar, L. Ungur, A. Valentini, S. Vancoillie, V. Veryazov, V. P. Vysotskiy, O. Weingart, F. Zapata, and R. Lindh, Molcas 8: New capabilities for multiconfigurational quantum chemical calculations across the periodic table, J. Comput. Chem. **37**, 506 (2016).

[63] A. A. Granovsky, Extended multi-configuration quasi-degenerate perturbation theory: The new approach to multi-state multi-reference perturbation theory, J. Chem. Phys. **134**, 214113 (2011).

[64] T. Shiozaki, W. Győrffy, P. Celani, and H.-J. Werner, Extended multi-state complete active space second-order perturbation theory: Energy and nuclear gradients, J. Chem. Phys. **135**, 081106 (2011).

[65] F. Neese, The ORCA program system, Comput. Mol. Sci. **2**, 73 (2012).

[66] H.-J. Werner, P. J. Knowles, G. Knizia, F. R. Manby, and M. Schütz, Molpro: A general-purpose quantum chemistry program package, Comput. Mol. Sci. **2**, 242 (2012).